Electronic Supplementary Material (ESI) for Energy .

Inverse Spinel $NiFeAlO_4$ as a Highly Active Oxygen Evolution Electrocatalyst: Promotion of Activity by a Redox-Inert Metal Ion

Jamie Y. C. Chen[†] Jeffrey T. Miller[‡], James B. Gerken[†], Shannon S. Stahl*[,†]

[†]Department of Chemistry, University of Wisconsin - Madison, 1101 University Avenue, Madison, WI 53706-1322, United States

[‡]Chemical Science, Engineering Division, Argonne National Laboratory, 9700 S. Cass Avenue, Argonne, Illinois 60439, United States

*Corresponding Author

E-mail: stahl@chem.wisc.edu

Telephone: (608) 265-6288; Fax: (608) 262-6143

Table of Contents

Experimental Section

1. Materials. $Ni(NO_3)_3$, $Fe(NO_3)_3$, $Al(NO_3)_3$ hydrates, and NaOH (99%) were purchased from Sigma Aldrich and used as received. Glassy carbon rotating disk electrodes (Pine Instruments) were sonicated in nitric acid for 2 hours prior to first use. An aqueous Ag/AgCl reference electrode (3 M NaCl) and Pt wire counter electrodes (BASi Analytical Instruments) were used. The Ag/AgCl reference electrode is regenerated in 3 M KCl after 2-3 experiments due to the corrosive nature of the alkaline conditions to the vycor tip. $K_3Fe(CN)_6$ (in pH 7 phosphate solution, $E_{1/2}$=225 mV vs. Ag/AgCl) was used to check the potential of the reference electrode after regeneration. Acetylene black conductive carbon powder is obtained from Soltex Inc. and treated with HNO_3 at 80 °C for 12 hours. Nafion (5 wt% in an alcohol solution) was purchased from Sigma Aldrich. Ultrapure water (Thermo-Scientific, 18 MΩ) was used for all solution preparations.

2. Catalyst Preparation. Oxide powders were prepared by nitrate combustion followed by calcination. In an alumina crucible, 1 M aqueous metal nitrate solutions containing 0.5 M glycine were mixed in the appropriate ratios. Combustion was carried out behind a blast shield on a hot plate at the highest setting, during which vigorous bubbling was observed with occasional sparking. In the case of NiO, a stainless steel mesh was used to cover the crucible to prevent powder dispersion into air. Subsequently, the dried powders were calcined at either 500 °C for 6 hours at 250 °C per hour (used for screening assay) or 1100 °C for 1 hour with a ramp at 998 °C per hour (the highest ramp rate of our furnace). The oxide was allowed to cool to room temperature inside the furnace.

3. Characterization. Powder X-ray diffraction patterns (pXRD) were recorded using Rigaku Rapid II system equipped with a 2-D imaging plate and Mo Kα X-ray tube (λ= 0.709Å) at room temperature. The detector was operated at 50 kV and 50 mA and scans were collected between the range of 5° - 45° with a step size of 0.01° and a sampling time of 0.3 s per step. Ground powder samples were mounted on a glass fiber using clear nail polish or vacuum grease as adhesive. The recorded patterns were matched to NiO (PDF#47-1049), $NiFe_2O_4$ (PDF#10-0325), and $NiAl_2O_4$ (PDF#1-1299) patterns from the ICDD database. Surface areas (3-trial average) were determined by the N_2-BET method. Measurements were collected using a Micrometrics Gemini VII 2390 Analyzer. Three measurements were collected for each oxide sample and standard deviation reported as the error. Particle images and elemental analysis were performed using a LEO 1530 scanning electron microscope (SEM) coupled with a Thermo-Fischer energy dispersive X-ray spectroscopy (EDX) detector.

4. Rietveld Refinement and XRD Simulation. Powder X-ray diffraction (XRD) for Rietveld refinement was performed on a D-8 Advance X-ray diffractometer with Cu Kα radiation (λ=1.54056 and 1.54439 Å, 1:0.5 ratio) at room temperature. XRD patterns were recorded between the range of 12-85° and 27.5-68.5° with a step size of 0.01° and a sampling time of 10 seconds per step. Rietveld refinement was done using EXPGUI and GSAS software.[1] Gaussian broadening parameters were obtained by fitting a NaCl diffraction pattern obtained on the same instrument over the same 2θ range with a step size of 0.01° and a sampling time of 7 seconds per step. Lorentzian broadening, U_{iso}, unit cell length, O position, and Fe and Al fractional occupancies were refined for both $NiFeAlO_4$ datasets together. Background, absorption, and sample translation, shift, and asymmetry parameters were refined for each sample independently. Additional structural models of the spinel oxides were constructed in VESTA and simulated powder patterns were created from the models using RIETAN-FP.[2,3] In these models, the nickel ions were ordered on sublattices within the octahedral sites. The best fit to the experimental data was achieved with Fd-3m symmetry, indicating disordered cation distribution within the O_h sites, compared to the ordering of the Ni occupancy of the octahedral sites in either $P4_122$ or Immb symmetry.[4]

5. Electrochemistry. All electrochemical experiments were performed using a standard three-component electrolysis cell with either a BASi Analytical Instrument or PINE Instrument Company potentiostat. *Catalyst ink* was prepared as follows: 2.5 mg of the oxide was mixed with 2.5 mg of acetylene black conductive carbon additive. Nafion (5 wt%, 0.15 mL, adjusted to pH 11 with 0.1 M NaOH) and 0.85 mL of H_2O:*i*PrOH in 80:20 ratio were subsequently added. Sonication of the ink for at least 30 minutes provided the necessary mixing, and 10 μL of ink was then deposited onto a glassy carbon (GC) rotating disk electrode. The ink deposit was removed by rinsing and sonication in methanol. The GC electrode was polished before each use with 0.5 μm alumina, followed by sonication in methanol to remove residual alumina. In all experiments, GC rotating disk (0.25 mm diameter), Ag/AgCl (in 3 M NaCl or KCl), and Pt wire were used as the working, reference, and counter electrode respectively. The electrolyte was a 0.1 M (pH 13) NaOH solution. All potentials were referenced to Ag/AgCl (0.209 V vs. NHE). *Cyclic voltammograms (CV)* were collected using scan rates of 50 and 1 mV/s *at the end of the Tafel experiments (after reaching steady state).* Ohmic resistances for CV experiments were correct using values measured by the BASi potentiostat. Prior to the collection of *Tafel data*, pre-electrolysis was performed at 0.7 V (vs. Ag/AgCl) until a steady current is observed. Tafel data were subsequently collected starting from 0.8 V vs. Ag/AgCl and decreased by 25 mV increments until the observed current fell below 10^{-7} A. Current was recorded at each applied potential until steady state was reached (typically 2 to 5 minutes), and the current averaged over the last 30 seconds was used to construct the Tafel plots. Ohmic resistances for the Tafel measurements were determined using method described by Kapałka et al.[5] *Determination of moles of redox active Ni-atoms* was based on the integration of the cathodic scan of the Ni^{II}/Ni^{III} feature of the cyclic voltammograms. These CVs were collected at a scan rate of 1 mV/s (see Fig. S4) after the completion of the Tafel experiments. Capacitance measurements were collected between 0.2 – 0.3 V (vs. Ag/AgCl), where no faradaic process is interfering, at scan rates of 30, 20, 10, 5, and 2 mV/s.

6. X-ray absorption spectroscopy. Fe (7.112 keV) and Ni (8.333 keV) K-edge X-ray absorption measurements were conducted on the bending magnet beamline of the Materials Research Collaborative Access Team (MRCAT 10-BM) at the Advanced Photon Source (APS) at Argonne National Laboratory. The X-ray ring at APS has a current of 102 mA and the beamline has a flux of 5 X 10^{10} photons/s. Ionization chambers were optimized for the maximum current with linear response (ca. 10^{10} photons detected s^{-1}). Catalyst samples were pressed into a cylindrical sample holder consisting of six wells, forming a self-supporting wafer. The catalyst amount used was calculated to give an absorbance (μx) of approximately 1.0 and data were collected in air at RT. The X-ray beam was 0.5 x 2.0 mm^2, and data were collected in transmission mode. A third detector in series simultaneously collected a Fe, or Ni foil reference spectrum with each measurement for energy calibration.

Powder X-ray Diffraction Spectrum

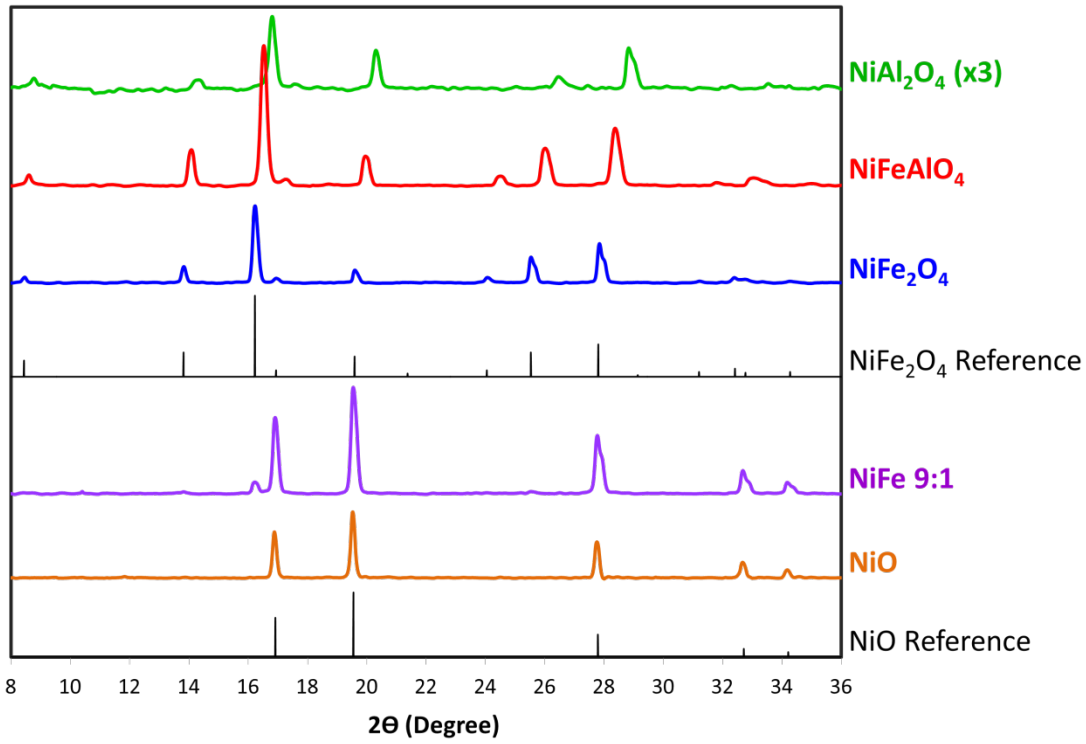

Figure S1. Mo Kα pXRD spectra of oxides examined for electrochemical activity. All oxides shown were prepared at 1100 °C. The intensity of the spectrum of $NiAl_2O_4$ has been expanded for easy comparison. Al_2O_3 phase was never observed. A small amount of $NiFe_2O_4$ is also observed in the spectrum of NiFe 9:1, in accordance with the literature.[6]

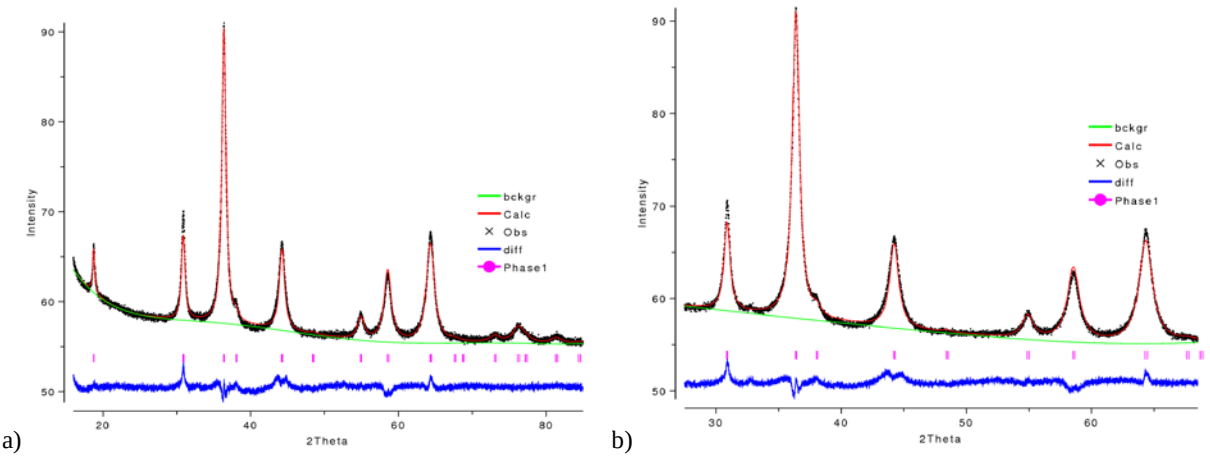

Figure S2. Cu Kα diffraction patterns of $NiFeAlO_4$ samples prepared as in Figure S1. Rietveld refined simulations are shown in red. a) $R_f^2 = 0.036$, b) $R_f^2 = 0.037$.

Scanning Electron Microscopy

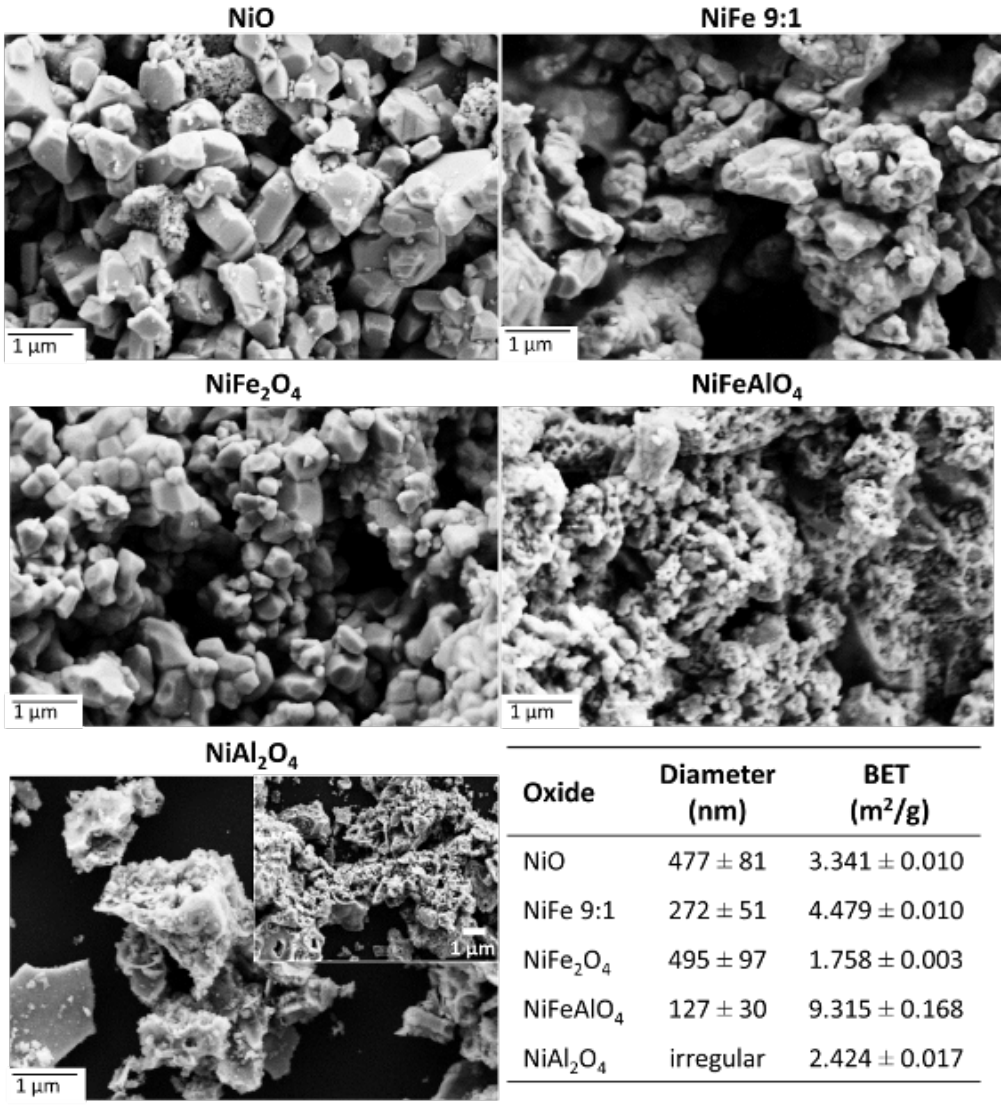

Oxide	Diameter (nm)	BET (m^2/g)
NiO	477 ± 81	3.341 ± 0.010
NiFe 9:1	272 ± 51	4.479 ± 0.010
$NiFe_2O_4$	495 ± 97	1.758 ± 0.003
$NiFeAlO_4$	127 ± 30	9.315 ± 0.168
$NiAl_2O_4$	irregular	2.424 ± 0.017

Figure S3. SEM images of the oxides with particle size and BET surface area measurements. NiO, NiFe 9:1, and $NiFe_2O_4$ exhibit highly facetted appearances, demonstrating their high crystallinity resulting from the high temperature calcination procedure. Oxides containing Al produced noticeably less facetted particles under identical preparation conditions, particularly $NiAl_2O_4$. The inset in the figure of $NiAl_2O_4$ shows a lower magnification view of the oxide. BET measurements showed low surface areas, consistent with the large particle sizes observed (diameters were averaged over 50 particles).

Cyclic Voltammogram Integration

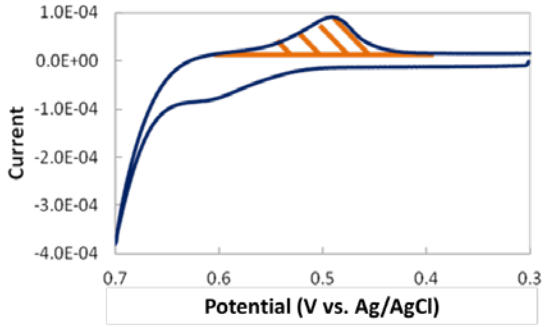

Figure S4. CV of $NiAl_2O_4$ illustrating the area integrated. The cathodic feature corresponds to the reduction of Ni^{III} to Ni^{II}. CVs were recorded at both 50 and 1 mV/s after the systems have reached steady state in 0.1 M NaOH using a glassy carbon rotating disk electrode. 1 mV/s CVs were used for integration. The feature from the cathodic scan was chosen due to its better separation from the catalytic wave. This is a valid method of counting the mole of active Ni atoms since the Ni^{II}/Ni^{III} redox feature is isolated from other redox events. It is has been shown that Fe_3O_4 exhibits no redox event at this range of potentials, thus we assumed no change in the oxidation state of Fe atoms.[7] This method of quantify the amount of active metal has also been reported previously.[8] This method of normalization was chosen for a couple reasons. For thin-film oxides directly interfaced with a working electrode, normalization using geometric or electrochemically active surface area is reasonable. For powder oxides, surface area measured by BET N_2-adsorption/desorption method is appropriate. However, metal oxide water oxidation catalysts have been shown to undergo significant structural changes under applied potential, resulting in an increase in surface area.[9] An additional method is to determine electrochemically active surface area via capacitance measurements. However, the significant amount of conductive carbon additive incorporated into the catalyst ink makes this approach unfeasible (Fig. S5).

Averaged Moles of Redox Active Ni

Table S1. Averaged moles of redox active Ni (< 1% of total Ni atoms present on electrode) in each oxide based on integration of the corresponding CV traces. Each reported value is an average of 3 trials.

	NiO	NiFe 9:1	$NiFe_2O_4$	$NiAl_2O_4$	$NiFeAlO_4$
Active Ni (mols)	9.39E-10 (± 5.6E-10)	12.3E-10 (± 0.78E-10)	1.88E-10 (± 0.35E-10)	5.95E-10 (± 2.5E-10)	18.5E-10 (± 3.1E-10)

Correlation between BET Surface Areas and Moles of Redox Active Ni

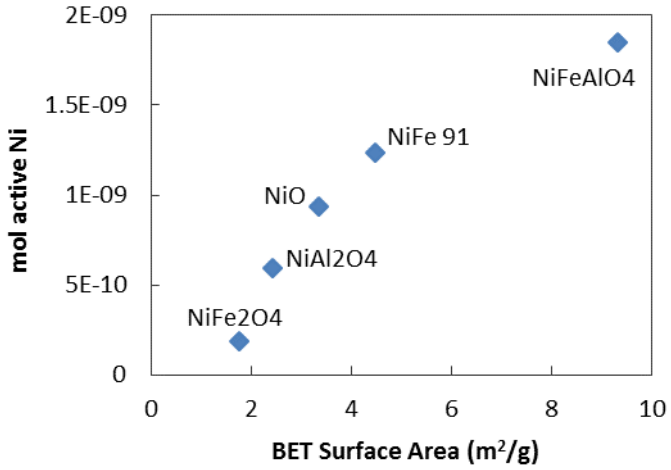

Figure S5. Correlation between the moles of redox active Ni (as determined by CV integration) and BET surface area. As BET surface area increased, a corresponding increase in the moles of redox active Ni was also observed.

Effect of Carbon Conductive Additive on Catalytic Activity and Capacitance

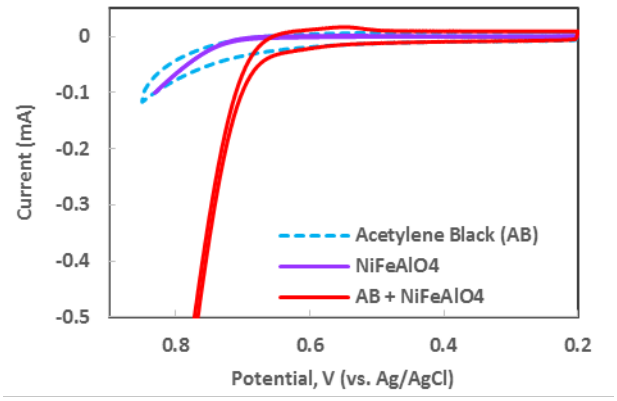

Figure S6. CV traces of acetylene black (AB), $NiFeAlO_4$, and [AB+$NiFeAlO_4$]. AB alone generated only low amounts of current due to its inability to oxidize water. $NiFeAlO_4$ alone also gave only low amounts of current due to insufficient electrical contact with the electrode. The combination of catalyst with AB resulted in a significant enhancement of observed current, illustrating the necessity of both the catalyst and conductive additive.

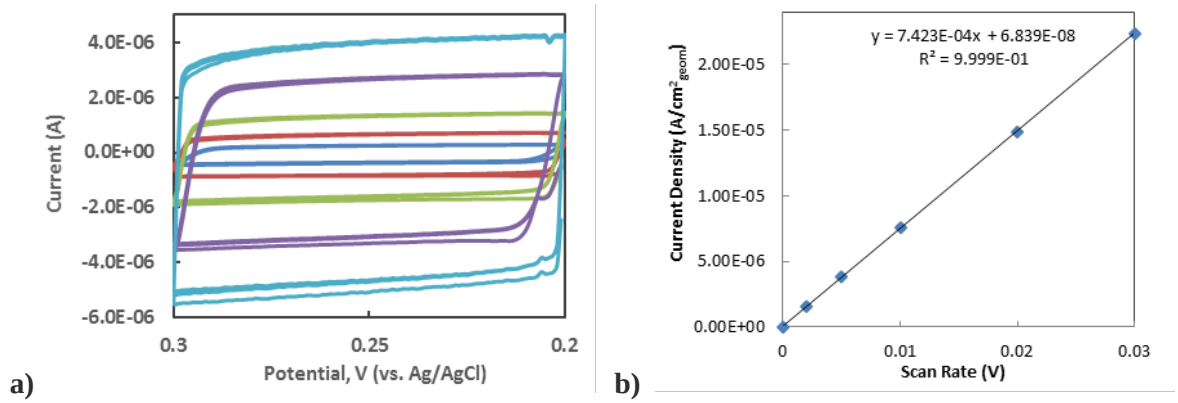

Figure S7. Example cyclic voltammetry and *i* – v plot of acetyene black, illustrating capacitance determination. CV collected was performed in a region where all catalysts showed no interfering redox processes (200 to 300 mV vs. Ag/AgCl). Varying the scan rate (v, 30, 20, 10, 5, 2 mV/s) produced different currents (Fig. S7-a), and the slope of the *i* - v plot (Fig. S7-b) gave the capacitance.

Table S2. Capacitance Measurements. The capacitance of the acetylene black (AB) carbon additive clearly dominates and the addition of $NiFeAlO_4$ catalyst did not result in any significant change of the capacitance. This observation shows that the determination of electrochemical surface area is infeasible. $NiFeAlO_4$ catalyst alone gave very low capacitance compared to AB, however, this measurement is problematic as the exclusion of AB resulted in insufficient electrical contact between the catalyst and the electrode (cf. Figure S6).

Averaged Capacitance (Farad)			
	$NiFeAlO_4$	**Acetylene Black**	**AB + $NiFeAlO_4$**
Pre-Electrolysis	9.56E-06 (± 1.30E-06)	1.40E-04 (±0.08E-04)	1.46E-04 (±0.05E-04)
Post-Electrolysis	2.45E-05 (± 0.39E-05)	1.78E-04 (±0.15E-04)	1.57E-04 (±0.09E-04)

BET Surface Area Normalized Tafel Plot and Tafel Slopes

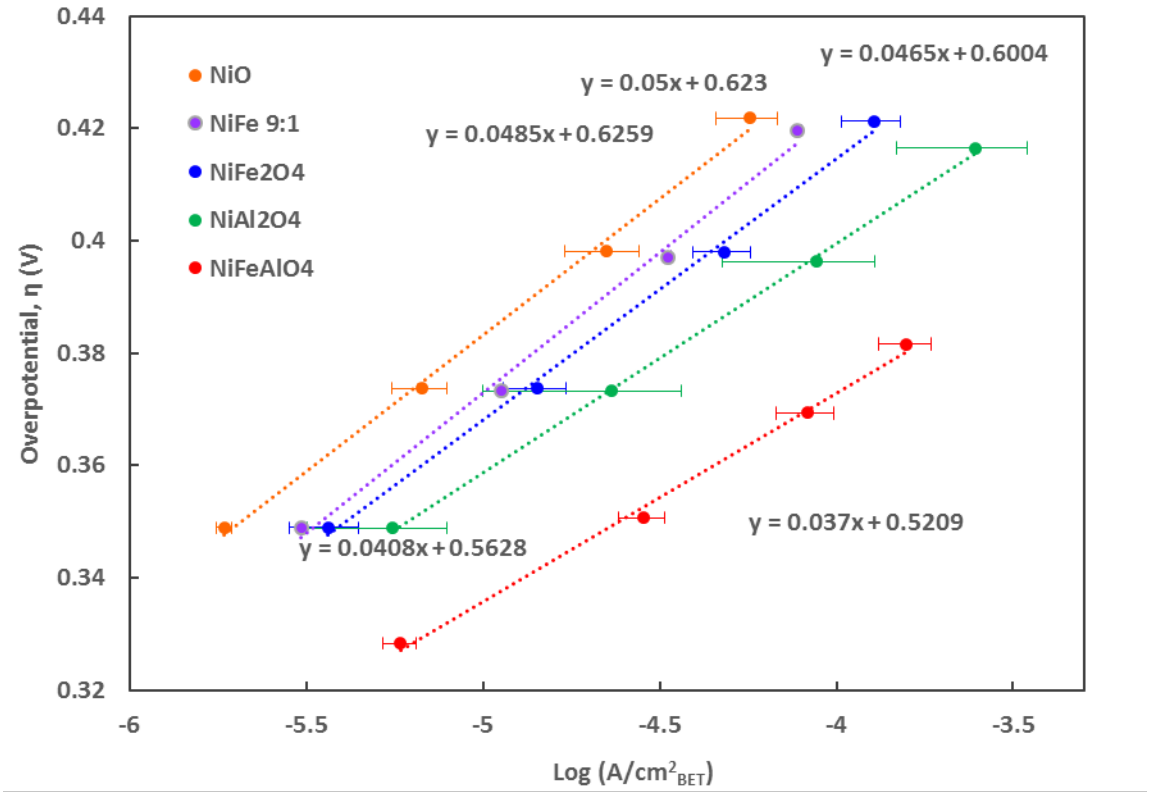

Figure S8. BET Surface area normalized steady-state electrocatalytic water oxidation activity. Tafel measurements were conducted in 0.1 M NaOH (pH 13) using a glassy carbon rotating disk electrode rotating at 1600 rpm. The error bar for NiFe 9:1 is small and hidden by the data symbol.

Tafel Slopes of the Oxides.

Table S3. Tafel slopes of the oxides examined (determined from BET surface area normalized Tafel plot) using all data points shown in Figure S8.

	NiO	NiFe 9:1	$NiFe_2O_4$	$NiAl_2O_4$	$NiFeAlO_4$
Tafel Slope (mV/dec)	49	50	47	41	37

Current Traces of the Individual Data Point on a Tafel Plot

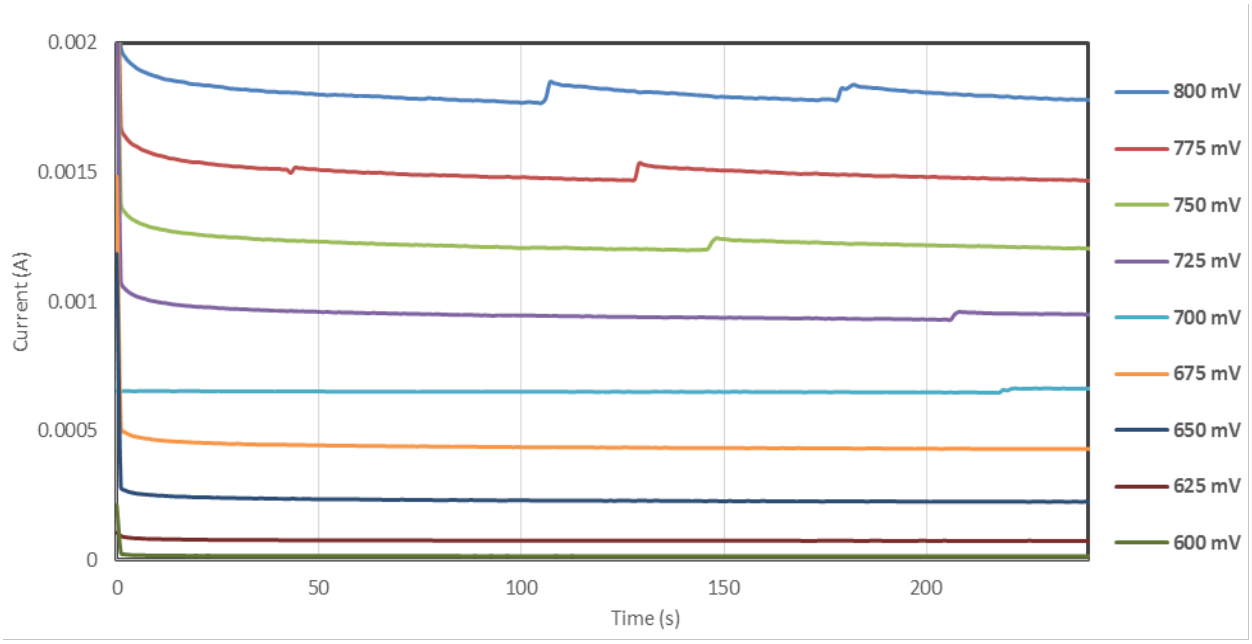

Figure S9. Example current trace of the steady-state measurement for $NiFeAlO_4$ at various applied potentials (vs. Ag/AgCl). The currents demonstrate catalyst stability during the acquisition of the Tafel data.

Oxygen Detection

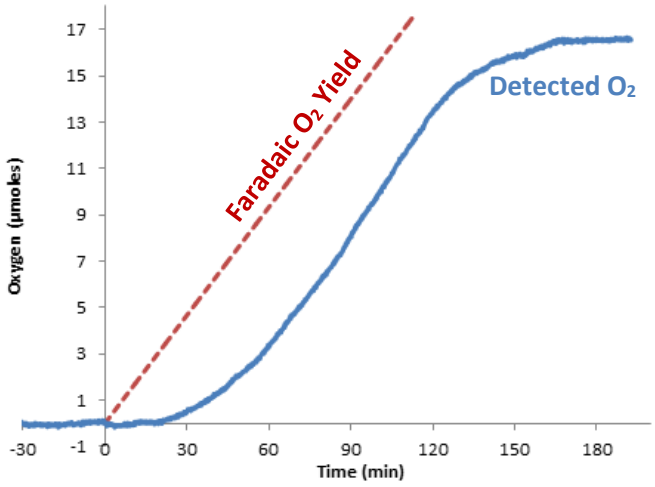

Figure S10. 94% Faradaic yield of O_2 was obtained after constant-current electrolysis for 112 minutes, indicating that the oxidation of conductive carbon additive is not a significant side reaction. The observed delay in the onset of O_2 detection is due to the time requried for O_2 to diffuse out of the electrolyte solution. Electrolysis was performed using an H-cell where 10 µL catalyst ink was deposited onto an FTO working electrode. Current density was fixed at 1 mA/cm^2_{geom} in 0.1 M NaOH (pH 13). Ag/AgCl (in 3 M KCl) and a Pt mesh were used as the reference and counter electrode, respectively. An Ocean Optic FOSPOR O_2 probe (O_2 sensitivity of 0 – 5%) was employed in the experiment.

EDS Ratiometric Analysis of $NiFeAlO_4$ Before and After an 15-hour Electrolysis

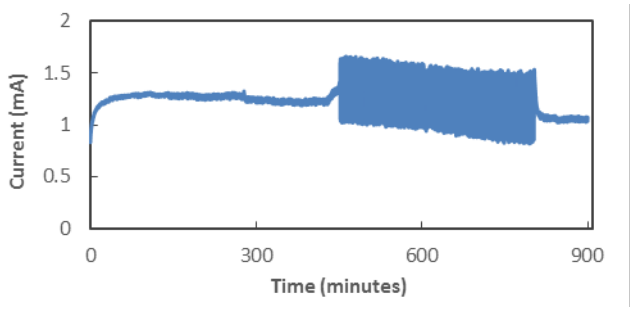

Figure S11. Electrolysis trace of $NiFeAlO_4$ in 0.1 M NaOH at 750 mV (vs. Ag/AgCl) over 15 hours. The RDE electrode was prepared as described previously. An approx. 20% decrease in current was observed, however it is unclear whether this is solely due to catalyst degradation or also contributions from the degradation of the conductive carbon and/or Nafion included in the ink deposit. The significant noise observed between 450 – 800 minutes was due to the electrode being partially covered by large bubbles, which occurred during the night.

Table S4. Elemental analysis of $NiFeAlO_4$ before and after electrolysis at 750 mV (see Fig. S11) for 15 hours showed no significant difference; reported values are the average of four areas of an oxide-covered glassy carbon electrode. All ratios are normalized to the amount of Ni (moles).

Element	Initial	Electrolyzed
Ni	1	1
Fe	1.02 ± 0.08	1.03 ± 0.06
Al	1.04 ± 0.15	1.21 ± 0.22

Table S5. Ni and Fe EXAFS Fittting Results

Ni and Fe EXAFS Fitting Results							
Sample	Pre-edge energy (keV)	Scatter	N	R, Å	$\Delta\sigma^2$ (x 10^3)	E_o, eV	Comments
NiO	8.3331	Ni-O	6.0	2.09	0.0	-0.3	Ni(II) XANES and Ni-O Standard
$NiAl_2O_4$ (1100 °C)	8.3331	Ni-O	6.1	2.05	0.0	-0.7	Ni(II)
$NiFe_2O_4$ (1100 °C)	8.3333	Ni-O	6.3	2.06	0.0	-1.2	Ni(II); Ni coordination similar to $NiAl_2O_4$
$NiFeAlO_4$ (1100 ºC)	8.3331	Ni-O	6.2	2.05	0.0	-1.4	Ni(II)
Fe_3O_4	7.1140	Fe-O	1.3	1.88	0.0	-5.5	XANES Standard
		Fe-O	4.1	2.07	0.0	2.4	
Fe_2O_3	7.1145	Fe-O	3.0	1.96	-3.0	-4.1	XANES and EXAFS Standard
		Fe-O	3.0	2.09	-3.0	1.1	
$NiFe_2O_4$ (1100 °C)	7.1140	Fe-O	1.8	1.87	-8.0	-4.4	Fe structure similar to Fe_3O_4
		Fe-O	3.4	2.04	-8.0	3.5	
$NiFeAlO_4$ (1100 °C)	7.1141	Fe-O	1.7	1.87	-5.0	-9.7	Fe structure similar to Fe_3O_4
		Fe-O	3.4	2.04	-5.0	9.6	

XAS spectra were analyzed using *WinXAS 3.1* software. The data were obtained from -250 eV below the edge to 1000 eV above the edge and normalized with linear and cubic fits of the pre-edge and post-edge regions, respectively. The oxidation state was obtained from the energy of the pre-edge peak and compared to respective reference compounds (i.e. NiO, Fe_3O_4, and Fe_2O_3). The pre-edge feature in Fe-edge spectra arise most prominently from tetrahedrally coordinated Fe atoms, which has an oxidation state of +3 in Fe_3O_4. The EXAFS was extracted by performing a cubic spline fit with 5 nodes from 2.5 to 13 $Å^{-1}$. The first-shell fits of the Fe and Ni coordination sphere (i.e., Fe-O and Ni-O) were obtained by fitting the Fourier transform of the k^2-weighted EXAFS from k = 2.6 – 11.5 $Å^{-1}$ and R = 1.0 -1.8 Å using experimental phase and amplitude functions obtained from NiO (6 Ni-O at 2.09 Å). The phase and amplitude of NiO, which is an excellent reference compound due to its high symmetry, were used to get a good fit for the Fe_2O_3 reference (3 Fe-O at 1.96 Å and 3 Fe-O at 2.09 Å). Scattering is proportional to the number of electrons in the adsorbing and scattering atoms. Since Ni^{+2} differs from Fe^{+3} by only three electrons, this small change is not enough to give a different phase and amplitude, and thus justifies the use of phase and amplitude generated from NiO. The Fe-O first shell coordination in Fe_2O_3 and Fe_3O_4 are different. Fe_3O_4 has 1 Fe atom in a T_d site with Fe-O distances of 1.88 Å and 2 Fe atoms in O_h sites with Fe-O distances of 2.07 Å. For Fe_3O_4, the fractional Fe occupancy of the T_d site is 0.33 (i.e., 1 of 3 sites), and the fractional Fe occupancy of the O_h sites is 0.667. The net Fe coordination number arising from the EXAFS fits reflects the weighted average of the Fe coordination numbers in the T_d and O_h sites:

Total T_d Fe-O bonds = 4
Total O_h Fe-O bonds = 2 x 6 = 12
Net Fe-O coordination number (N) = [4 (T_d) + 12 (O_h)]/3 Fe atoms = **5.33 Fe-O**

Using the known bond distances for T_d and O_h in Fe_3O_4, fits were adjusted to give the correct Fe-O coordination numbers for this reference material. The T_d and O_h Fe-O bond distances in $NiFe_2O_4$ are 1.88 and 2.07 Å, respectively, based on XRD data (ICSD Collection Code: 157691). In the fits used to determine the Fe occupancy of the T_d and O_h sites of the unknown samples (e.g., $NiFe_2O_4$ and $NiFeAlO_4$) these bond distances were held constant. Several Fe-O T_d and O_h coordination numbers gave acceptable fits to the EXAFS data. The fraction of Fe in a T_d site is the T_d Fe-O coordination number divided by 4 and similarly the fraction of Fe in an O_h site is the O_h Fe-O coordination number divided by 6. Correctly fitted Fe-O coordination numbers were those that resulted in a total fraction of T_d and O_h Fe equaling to 1.0 (i.e., all

the Fe in the sample). For $NiFe_2O_4$ and $NiFeAlO_4$ the Fe occupancy of the T_d and O_h sites was very similar at about 0.45 T_d and 0.55 O_h (compared to 0.33 T_d and 0.66 O_h in Fe_3O_4), which is consistent with the replacement of one octahedrally coordinated Fe by Ni atom.

Ni-Edge XAS Spectra

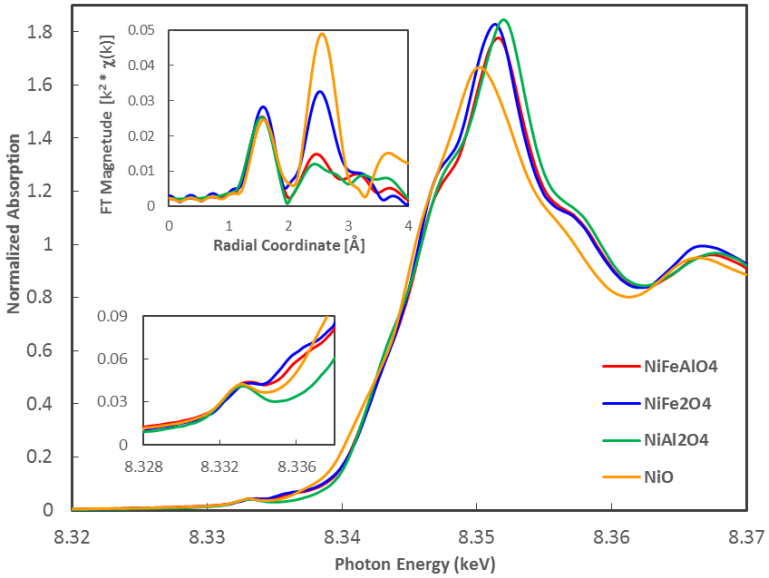

Figure S12. Ni-edge XAS spectrum of NiO, $NiFe_2O_4$, $NiFeAlO_4$, and $NiAl_2O_4$. The edge positions of the inverse spinel oxides are 0.7 eV higher than that of NiO but lower than Ni^{III}, such as β-NiOOH, which is another 0.9 eV higher at 8343.7 eV.[10] The XANES edge is an allowed transition from the 1s to unfilled p states, thus the edge energy varies substantially with the types of ligands present. A more reliable determination of the oxidation state of the Ni uses the small pre-edge peak (about 8.333 keV, see lower insert). This peak is due to the dipole forbidden transition from the 1s to 3d orbitals, which is very characteristic of the oxidation state. The weak appearance of the pre-edge feature seen here is a result of the highly symmetric environment surrounding the octahedral Ni centers. A peak cooresponding to Ni-O coordination (1.6 Å of the phase-uncorrected radial coordinate) in the EXAFS region overlaps between the inverse spinel oxides and NiO (upper insert). Since all Ni atoms are octahedrally coordinated in NiO, this observed overlap indicates that the Ni atoms in the inverse spinels are largely, if not completely, octahedrally coordinated. In the Ni-O-M coordination sphere, much reduced intensities are observed in the in the Al-containing inverse spinel oxides, reflecting the lower scattering ability of the Al atom compared to Ni and Fe.

1 a) A. C. Larson and R. B. Von Dreele, "General Structure Analysis System (GSAS)", Los Alamos National Laboratory Report LAUR 86-748 (2000); b) B. H. Toby, *J. Appl. Cryst.*, 2001, **34**, 210-213
2 K. Momma and F. Izumi, *J. Appl. Crystallogr.* 2011, **44**, 1272 - 1276
3 F. Izumi and K. Momma, *Solid State Phenom.* 2007, **130**, 15 - 20
4 For discussion of cation ordering in inverse spinels, see: C. Haas, *J. Phys. Chem. Solids*, 1965, **26**, 1225 - 1232
5 A. Kapałka, G. Foti and C. Comninellis, *Electrochem. Comm.*, 2008, **10**, 607-610
6 J. Landon, E. Demeter, N. İnoğlu, C. Keturakis, I. E. Wachs, R. Vasić, A. I. Frenkel and J. R. Kitchin, *ACS Catal.*, 2012, **2**, 1793-1801
7 K.-S. Jung and L. de Pierrefeu, *Corros. Sci.* 2010, **52**, 817-825
8 T. Nakagawa, C. A. Beasley and R. W. Murray, *J. Phys. Chem. C*, 2009, **113**, 12958-12961
9 K. J. May, C. E. Carlton, K. A. Stoerzinger, M. Risch, J. Suntivich, Y.-L. Lee, A. Grimaud and Y. Shao-Horn, *Phys. Chem. Lett.* 2012, **3**, 3264-3270
10 D. K. Bediako, B. Lassalle-Kaiser, Y. Surendranath, J. Yano, V. K. Yachandra and D. G. Nocera, *J. Am. Chem. Soc.* 2012, **134**, 6801-6809